A gel-forming clusteroluminogenic polymer with tunable emission behavior as a sustained-release carrier enabling real-time tracking during bioactive agent delivery

Abstract

Sustained-release carriers with intrinsic luminescence exhibit the potential to combine imaging with bioactive agent delivery in practice. This study reports the synthesis and properties of CT, which is a gel-forming and highly tunable non-conjugated polymer with intrinsic luminescence. Owing to the excitation wavelength-dependent emission tunability of CT, optical imaging can be performed in a wide range of excitation wavelengths. This study is the first proof-of-concept study successfully integrating the property of clusterization-triggered emission into carrier design for combining imaging with bioactive agent delivery. By using cancer therapy as a practical example, our results demonstrate that CT is a depot system that cannot only enhance *in vivo* antitumor efficacy but can also allow its location and gelation process to be tracked in real time by giving an intrinsic blue-colored fluorescence signal. Together with its high biocompatibility, CT shows high practical potential for executing self-illuminating therapy to tackle cancer.

1. Introduction

Sustained-release carriers with high luminescence show the potential to combine imaging with bioactive agent delivery in practice. Different luminescent systems have been reported in the literature, ranging from metal nanoclusters [1] and upconversion nanoparticles [2,3] to luminescent polymers [4]. Among them, luminescent polymers have drawn special interest partly because of their structural flexibility and ease of functionalization for subsequent property modification. Over the years, diverse carriers have been developed from luminescent polymers [5,6], rendering the combination of imaging with bioactive agent delivery possible. Despite this, luminescence from these polymers necessitates the availability of π-conjugated systems. Due to the presence of the rigid planar structure inherently linked to the conjugated electronic system [7], these polymers experience aggregation-caused quenching easily when they are in high concentration [7]. In addition, owing to the need of extended conjugation (and hence higher structural complexity) in the structure of these polymers, laborious synthetic procedures are often involved. All these factors impose limitations on the working concentration and large-scale production of these polymers for use in bioactive agent delivery.

To address these problems, readily-fabricated luminescent polymers enabling high flexibility of structural design are desired. By taking advantage of the mechanism of clusterization-triggered emission (CTE), this study develops a novel gel-forming non-conjugated luminescent polymer, namely CT. Because of its luminescence properties and excitation wavelength-dependent emission tunability, CT enables its location and *in situ* gelation process inside a body to be tracked in real time, with the imaging process being able to be performed in a wide range of excitation wavelengths based on practical needs. Importantly, due to the lack of conjugated electronic structures, CT is structurally

flexible, and can serve as an *in situ* gel-forming depot system for sustained and controlled release of the loaded agent. Such structural flexibility can hardly be achieved by existing carriers that are developed conventionally from polymeric luminogens with rigid π-conjugated structures. By using cancer therapy as a practical example, CT is demonstrated to show high potential to mediate the execution and development of self-illuminating therapy in disease treatment due to its high biocompatibility, release sustainability and *in situ* gel-forming capacity which can spare the need of subsequent gel implantation.

2. Materials and methods

2.1. Materials

4-Dimethylaminopyridine (DMAP), 1-chloro-2,3-epoxypropane, 2-methylpropenoic acid, and various other chemicals were purchased from Sigma-Aldrich (St. Louis, MO, USA). Cellulose modified simultaneously by hydroxypropylation (degree of substitution = 7–12%) and methylation (degree of substitution = 28–30%), with the viscosity of its 2% aqueous solution at ambient conditions being 6, 15, or 50 mPa·s (designated as CE06, CE15, and CE50, respectively), was purchased from Macklin (Shanghai, China). Dulbecco's Modified Eagle's Medium (DMEM; Gibco, Grand Island, USA), RPMI-1640 (Gibco, Grand Island, USA), penicillin G-streptomycin sulfate (Life Technologies Corporation, Chicago, USA), and fetal bovine serum (FBS; Hangzhou Sijiqing Biological Engineering Materials Co, Hangzhou, China) were used as the cell culture medium. Trypsin-EDTA (0.25% trypsin-EDTA) was obtained from Invitrogen (Carlsbad, CA, USA).

2.2. Synthesis of CT

100 mL of 2-methylpropenoic acid was added to 100 mL of heptane, followed by the dropwise addition of 200 mL of a 50% (w/v) NaOH solution at 55 °C under constant stirring. After 30 min of reaction at 55 °C, 0.2 g of hydroquinone was added. The product was purified by vacuum distillation. 40 g of the product was added to a flask equipped with a reflux condenser and a $CaCl_2$ tube, followed by the addition of 0.2 g of pre-desiccated hydroquinone, 1.2 g of pre-desiccated tetrabutylammonium bromide, and 285 mL of 1-chloro-2,3-epoxypropane under constant stirring. The reaction mixture was heated at 90–95 °C on a water bath for 4 h, and was then cooled to room temperature.

The crude reaction mixture was filtered, with the filtrate further purified by vacuum distillation to obtain a product in the form of a colorless mobile liquid. 2 mL of the product was added dropwise to 45 mL of an anhydrous DMSO solution containing both CE06 (5.6% (w/v)) and DMAP (1.1% (w/v)). The reaction mixture was incubated under the inert nitrogen atmosphere for 72 h. After that, the reaction mixture was dialyzed against deionized water for 3 days with a molecular weight cut-off of 12 kDa. The dried product was obtained by lyophilization, and was stored at 4 °C for subsequent use. The same procedure was applied to CE15 and CE50 to generate CT with different molecular weights. CT generated from CE06, CE15, and CE50 was designated as CT06, CT15, and CT50, respectively.

2.3. Structural characterization

The structure of CT was characterized by using a Fourier-transform infrared (FT-IR) spectrometer (Spectrum 2000; PerkinElmer, Norwalk, CT, USA) at ambient conditions. The potassium bromide (KBr) disk technique was used for analysis. Spectra were obtained at a resolution of 2 cm^{-1}, and were reported as an average of 16 scans. In addition, CE06, CE15, CE50, CT06, CT15 and CT50 were solubilized in deuterated DMSO (DMSO-d_6). Their proton nuclear magnetic resonance (^{1}H NMR) spectra were recorded using an NMR spectrometer (400 MHz; Bruker Corporation, Karlsruhe, Germany).

2.4. Gel permeation chromatography (GPC)

100 mg of CT06, CT15 or CT50 was dissolved in 10 mL of tetrahydrofuran (THF), which was used as a mobile phase during subsequent GPC analysis. Dissolution of CT was facilitated by sonication for 10 min. During analysis, the flow rate of the mobile phase was set as 1.0 mL min^{-1}. Detection was achieved by using a refractive index detector at ambient conditions.

2.5. Thermogravimetric analysis (TGA)

TGA of CE06, CE15, CE50, CT06, CT15 and CT50 was performed using a Q50 TGA analyzer (TA Instruments, New Castle, Delaware, USA) equipped with platinum pans. Analysis was carried out in an inert atmosphere of nitrogen from 40 °C to 600 °C. The heating rate was uniform in all cases, and was set as 10 °C min^{-1}.

2.6. Scanning electron microscopy (SEM) analysis

The microstructure of a lyophilized gel formed from CT was examined by SEM. Slices of the lyophilized gel were sputter-coated with gold, and were observed using a scanning electron microscope (JSM-6380; JEOL, Tokyo, Japan) operated at an accelerating voltage of 10 kV.

2.7. Rheological measurement

The viscosity of a 5% (w/v) DMSO solution of CT before and after injection into simulated body fluid, which was prepared as previously described [8], was determined using a Brookfield DV-III Ultra programmable rheometer (Brookfield Engineering Laboratories Inc., Middleboro, MA, USA) with spindles (CP-40). Viscosity parameters were collected at different shear rates at ambient conditions, with the equilibration time at every shear rate being set as 15 s. Viscoelastic properties of a 5% (w/v) DMSO solution of CT and the gel formed were also studied in the frequency range of 1–100 rad s^{-1}. The storage modulus (G') and loss modulus (G'') were determined.

2.8. Evaluation of the swelling behavior

A lyophilized and pre-weighed gel (0.05 g) was immersed in 100 mL of simulated body fluid. At a pre-set time interval, the sample was retrieved by centrifugation for 5 min at a relative centrifugal force of 4000 × g, followed by the removal of the supernatant. The

swelling ratio, the water content, and the water absorption ratio (WAR) of the sample were calculated using the following equations:(1)Swellingratio=msmd(2)Watercontent(%)=ms−mdms×100%(3)WAR=ms−m dmdwhere m_s and m_d represent the mass of the swollen gel and that of the dried gel, respectively.

2.9. Evaluation of the erosion behavior

The erosion behavior of a gel formed from CT was examined as previously described [9]. In brief, a lyophilized gel with a known initial dry mass was immersed in simulated body fluid, and was incubated at 37 °C. The sample was retrieved at a predetermined time interval, and was dried in an oven at 65 °C. The final dry mass of the gel was determined.

2.10. Cytotoxicity assay

3T3 mouse fibroblasts were cultured in DMEM supplemented with 10% FBS, 100 UI/mL penicillin, 100 μg/mL streptomycin, and 2 mM L-glutamine; whereas BGC-823 cells were cultured in RPMI-1640 supplemented with 10% FBS. 24 h before the assay, cells were seeded separately in a 96-well plate at an initial density of 5000 cells per well, and were incubated under a humidified atmosphere of 5% CO_2 at 37 °C. On the other hand, an appropriate amount of CT was ground in the fresh cell culture medium using mortar and pestle to obtain a suspension with a desired CT concentration. During the experiment, the cell culture medium in each well was replaced with 100 μL of the suspension. After 5 h incubation at 37 °C, the suspension was replaced with the fresh cell culture medium. The CellTiter 96 AQueous non-radioactive cell proliferation assay (MTS assay; Promega Corp., Madison, WI, USA) was performed, according to the manufacturer's instructions, either immediately or after 24 h of post-treatment incubation to determine the cell viability (%) in each well.

2.11. Blood collection and hemolysis assay

Blood from anesthetized nude mice was collected via cardiac puncture into a heparin-containing tube, and was then centrifuged for 10 min at 2000 × g at 4 °C. All procedures were approved by the Ethical Committee of the Hong Kong Polytechnic University. The collected erythrocytes were washed with phosphate buffered saline (PBS) (pH=7.4) until the supernatant became colorless. Different amounts of CT were ground in PBS using mortar and pestle. The solutions obtained were filtered using a microfilter with a pore size of 0.45 μm. Erythrocytes were added to the filtrates to reach a final concentration of 8% (v/v). After incubation at 37 °C for 1 h, the mixtures were centrifuged at a relative centrifugal force of 2000 × g for 15 min. The absorbance of the supernatants was recorded at 414 nm. Experiments were performed in triplicate. The extent of hemolysis in PBS and 0.1% (w/v) Triton X-100 was defined as 0% and 100%, respectively.

2.12. Photoluminescence (PL) characterization

0.5 g of CT was dissolved in 10 mL of DMSO for measurements using a FLS920P fluorescence spectrometer (Edinburgh Instruments Ltd., Livingston, UK). PL spectra were taken at excitation wavelengths of 330 nm, 340 nm, 350 nm, 360 nm, 370 nm, 380 nm,

390 nm, 400 nm, 410 nm, 420 nm, and 430 nm. PL lifetime measurements were recorded when the sample was excited by a 375 nm pulsed laser (Edinburgh Instruments EPL-375) with a pulse rate of 500 ns.

2.13. Determination of the encapsulation efficiency

Methylene blue (MB), lysozyme (LYS), capecitabine (CAP), and paclitaxel (PTX) were adopted as model agents. 0.2 g of the agent was dissolved in 4 mL of a 5% (w/v) DMSO solution of CT. The solution was injected into 25 mL of simulated body fluid for *in situ* gel formation. The agent-loaded gel was retrieved by centrifugation for 30 min at a relative centrifugal force of 10,000 × g, followed by the removal of the supernatant. The concentration of unloaded MB was determined at 665 nm using ultraviolet–visible (UV–Vis) spectroscopy. The amount of unloaded LYS was determined using the Bradford reagent (Sigma-Aldrich, Missouri, USA) as previously described [10]. The concentrations of CAP and PTX were quantified using reverse phase ultra-high performance liquid chromatography (UPLC), coupled with a triple quadrupole mass spectrometer (UPLC-MS/MS). The encapsulation efficiency was calculated using the following equation:(4)Encapsulationefficiency(%)=mlmt×100%where m_l is the mass of the model agent encapsulated in the gel, and m_t is the total mass of the model agent added during the encapsulation process.

2.14. Evaluation of release performance

25 mL of simulated body fluid was added as a releasing medium to 0.2 g of a lyophilized agent-loaded gel, and was incubated at 37 °C with saturated humidity. At a pre-set time interval, 0.5 mL of the releasing medium was removed for testing, and was replaced with 0.5 mL of simulated body fluid. The amount of MB released from the gel was determined at 665 nm using UV–Vis spectroscopy. The amount of LYS released was determined using the Bradford reagent as previously described [10]. The concentrations of PTX and CAP in the releasing medium were measured by using UPLC-MS/MS. The cumulative payload release was calculated using the following equation:(5)Cumulativerelease(%)=∑t=0tmtm∞×100%where m_t is the mass of the model agent released from the gel at time *t*, and m_∞ is the total mass of the model agent loaded into the gel.

2.15. Determination of the protein activity

A LYS-loaded gel was prepared as described above, and was crushed thoroughly using mortar and pestle in PBS. After removing the debris by filtration, the amount of LYS extracted from the gel was determined using the Bradford reagent. 100 μL of the solution containing extracted LYS was added to a cuvette, followed by the addition of 1 mL of a 0.01% (w/v) *Micrococcus lysodeikticus* cell suspension. The absorbance at 450 nm was measured to determine the activity of extracted LYS.

2.16. Evaluation of use in self-illuminating antitumor therapy

BALB/c nude mice (5 weeks of age) were purchased from the Institute of Laboratory Animal Sciences (Beijing, China). BGC-823 cells were cultured in RPMI-1640

supplemented with 10% FBS. All procedures were approved by the Ethical Committee of the Hong Kong Polytechnic University. A BGC-823 cell suspension prepared in 0.2 mL of a PBS/Matrigel mixture (1:1) at a concentration of 1×10^7 cells mL^{-1} was transplanted subcutaneously into the nude mice to produce tumors. The tumor volume (*V*) was determined using a caliper, and was calculated using the following equation:(6)V=12×L×S2where *L* is the larger dimeter of the tumor, and *S* is the small diameter of the tumor. When the tumor reached a volume of 100 mm^3, the mice were weighed, coded, and randomly divided into 4 groups, with 7 mice in each group. Intratumoral administration of the CT15 solution, the PTX solution, or the PTX-containing CT15 solution, was provided twice a week for 2 weeks. The dose of PTX administered each time was 20 mg kg^{-1}. In all cases, the solvent used was DMSO, which was selected in this study partly because of its track record of use in direct injection in preclinical trials [11,12] and its high miscibility with body fluid [13]. Intratumoral administration of the solvent alone was used as the control. Dynamic changes in the tumor volume were determined. After 2 weeks of treatment, mice were sacrificed, with their tumors excised and weighed. The tumor growth inhibition (TGI) value was determined using the following equation:(7)TGI(%)=(1−WTWC)×100%where W_T is the average tumor weight in the treatment group, and W_C is the average tumor weight in the control group. Sections of tumors were examined by hematoxylin and eosin (H&E) staining. Proliferating cell nuclear antigen (Ki67) staining was used to determine cell proliferation. Apoptotic nuclear DNA breaks in the tissue sections were assessed by both terminal dUTP nick-end labeling (TUNEL) and 4,6-diamidino-2-phenylindole (DAPI) labeling.

2.17. Real-time tracking of the gel

Mice were injected via intraperitoneal (IP) injection with 500 μL of a 5% (w/v) DMSO solution of CT15 using an 18-gauge needle. All procedures were approved by the Ethical Committee of the Hong Kong Polytechnic University. After injection, fluorescence imaging was performed using the FocusBio iKon *In Vivo* Imaging System (ColdSpring, Beijing, China) at a pre-set time interval. Automatic settings were used for all imaging procedures (λ_{ex} = 435 nm; λ_{em} = 609 nm). The *in vivo* fluorescence signal of the gel formed from CT was analyzed using the BioAnalysis software package. The same procedure was applied to image the gel formed upon intratumoral injection of a 5% (w/v) DMSO solution of CT15 containing PTX to nude mice with gastric cancer xenografts.

2.18. Statistical analysis

All data were expressed as the means ± standard deviation. Unless otherwise specified, the mean value was obtained by averaging five replicates. Student's *t*-test was performed to assess the statistical significance. Differences with p-value < 0.05 were considered to be statistically significant. Statistical analysis was performed using GraphPad Prism 8.2.0 software (GraphPad Software Inc., San Diego, CA, USA).

3. Results and discussion

3.1. Synthesis and structural characterization of CT

Generation of CT starts from hydroxypropylation and methylation of cellulose, followed by transesterification which is facilitated by the use of a polar aprotic solvent as the reaction medium (Fig. 1A). CT with various molecular weights (32.6 kDa, 47.8 kDa, and 52.7 kDa) is synthesized. The polymers are designated as CT06, CT15, and CT50, respectively. The yields of these polymers are approximated to be 45.2%, 55.1% and 65.3%, with their polydispersity index (PDI) values being 1.77, 1.73 and 2.04, respectively (Fig. 1B-C). The structure of CT is examined using FT-IR spectroscopy (Fig. 1D). The peak at 1730 cm^{-1} in the spectra of CT is attributed to the carbonyl signal from the methacrylate group (C=O stretching). Compared to the spectra of CE, those of CT show stronger signals in the wavenumber range between 2850 and 3000 cm^{-1}. These signals are assigned to C—H stretching vibrations. The amplification of the signals in the spectra of CT is attributed to the supplementary CH_3 groups from methacrylate groups. The structure of CT is further characterized using ^1H NMR (Fig. 1E), in which peaks at around 5.7 and 6.2 ppm are observed in the spectra of CT but not in the spectra of CE. These peaks are characteristic of protons from the double bond in the methacrylate group.

(A)

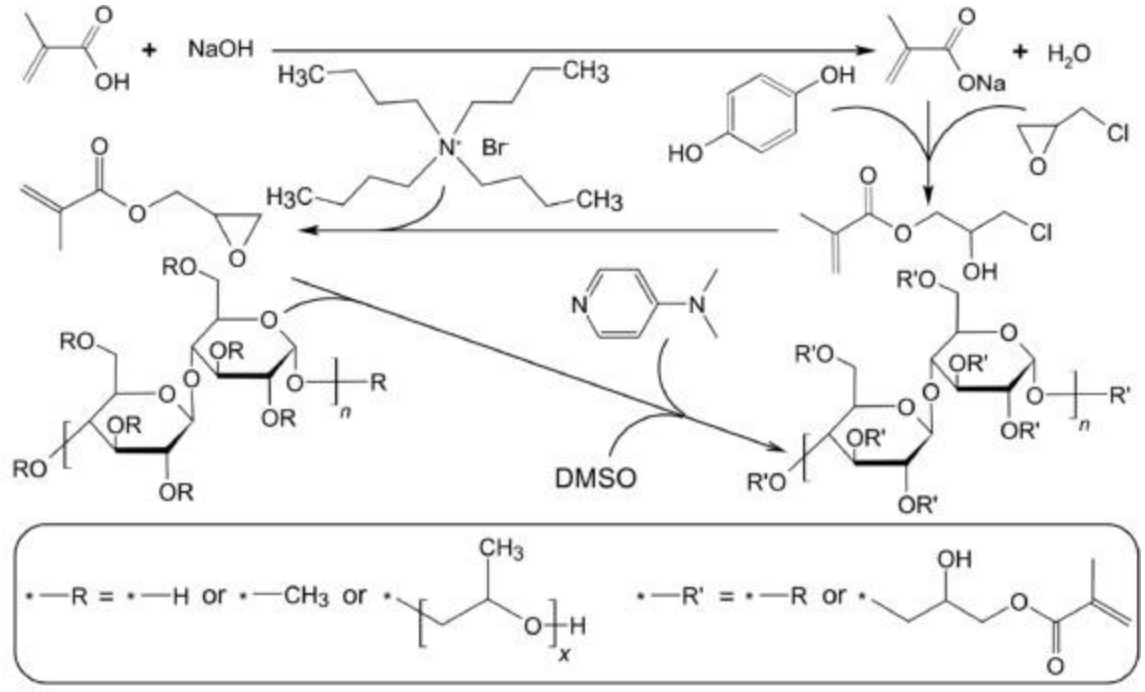

(B)

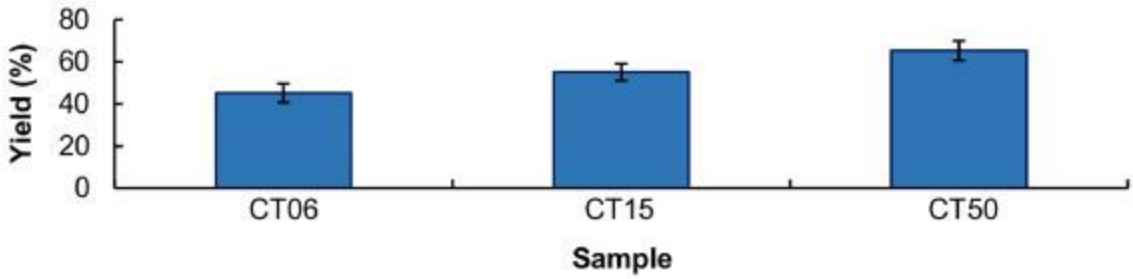

(C)

Sample	M_n (Da)	M_w (Da)	M_P (Da)	M_z (Da)	M_{z+1} (Da)	PDI
CT06	8391	32637	26802	57159	91959	1.774650
CT15	27639	47755	45857	79304	117279	1.727803
CT50	25792	52707	49063	95202	145100	2.043506

(D)

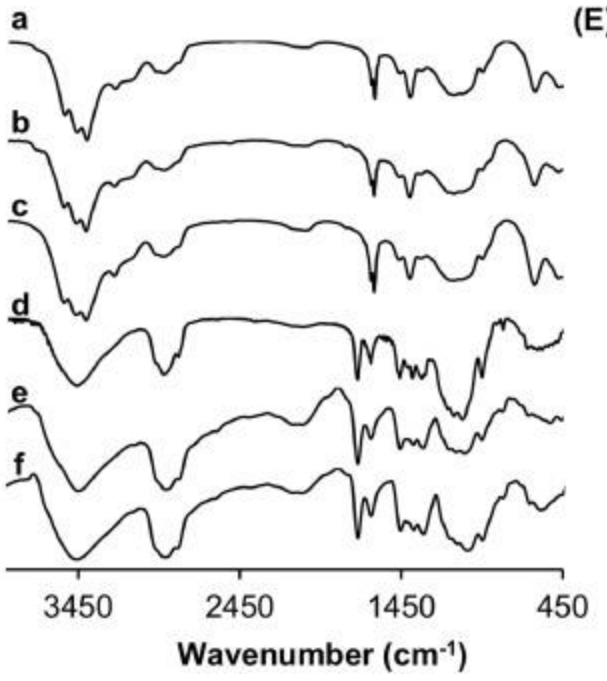

(E)

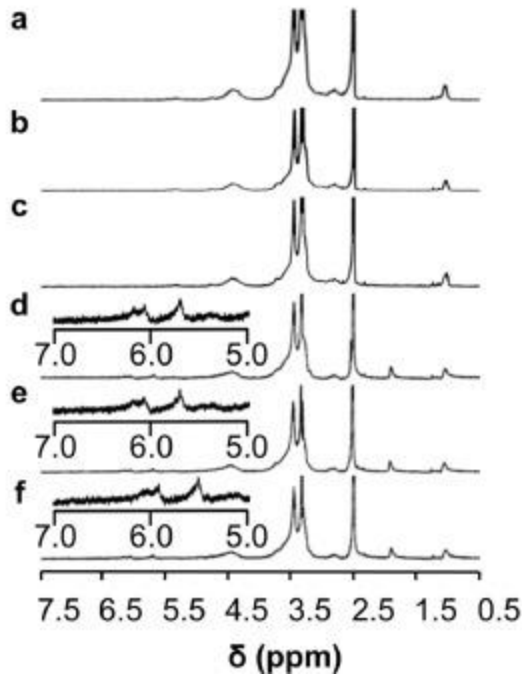

Fig. 1. Synthesis and structural characterization of CT. (A) A schematic diagram showing the synthetic process of CT. (B) Yield percentages of different CT samples. (C) The molecular weights of different CT samples as determined by GPC. (D) FT-IR spectra of (a) CE06, (b) CE15, (c) CE50, (d) CT06, (e) CT15, and (f) CT50. (E) ^{1}H NMR spectra of (a) CE06, (b) CE15, (c) CE50, (d) CT06, (e) CT15, and (f) CT50.

The thermal behavior of CT is studied by TGA. The curves of CE06, CE15 and CE50 suggest that they are thermally stable up to 260 °C, after which thermal decomposition occurs, showing a significant reduction in the weight percentage between approximately 266 and 394 °C ($\Delta m = 82.45\%$) (Fig. 2A). There is a slight increase in the thermal decomposition temperature as the molecular weight of CT increases. The process of transesterification for the production of CT has led to no observable change to the thermal property of CE.

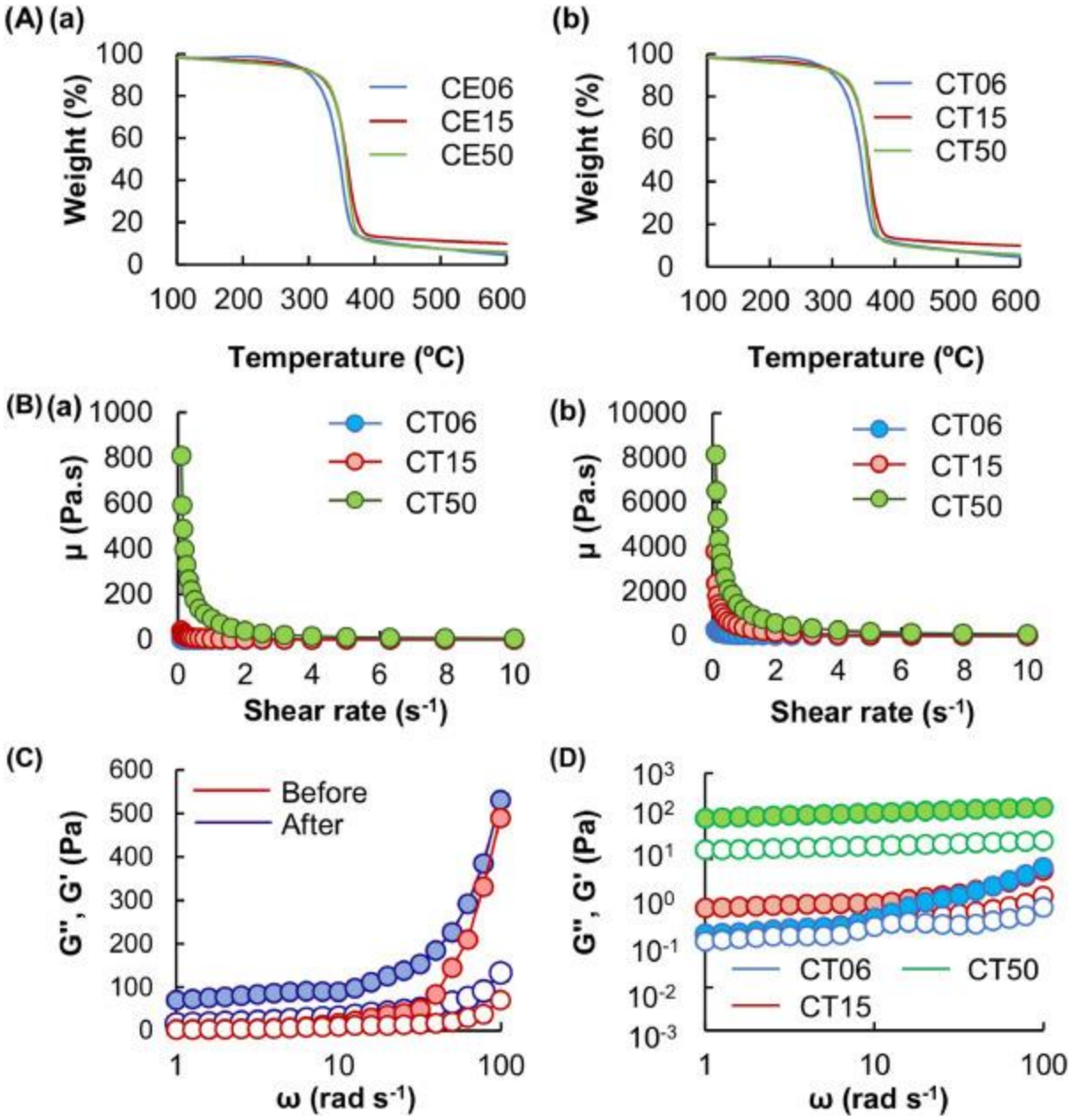

Fig. 2. Thermal and rheological properties of CT. (A) TGA curves of (a) CE06, CE15 and CE50, as well as those of (b) CT06, CT15, CT50. (B) Viscosity curves of DMSO solutions of CT with different molecular weights. Measurements were made (a) before and (b) after injection of the solutions into simulated body fluid. (C) Changes in G'' and G' values from 1 to 100 rad s^{-1} before and after injection of the DMSO solution of CT15 into simulated body fluid. Solid dots represent G' values and unfilled dots denote G'' values. (D) Changes in G'' and G' values from 1 to 100 rad s^{-1} experienced by the gels formed from DMSO solutions of CT with different molecular weights. Solid dots represent G' values and unfilled dots denote G'' values.

3.2. Rheological properties and microstructural tunability

The viscosity of the DMSO solutions of CT is shown in Fig. 2B. The apparent viscosity of all of the CT solutions, before and after injection into simulated body fluid, is higher at a low shear rate than at a high shear rate. This indicates that the polymers, as well as the gels formed, exhibit pseudoplastic behavior. An increase in the molecular weight of CT facilitates the entanglement of the molecules, thereby enhancing the extent of inter-molecular interactions and hence the viscosity of the solution. Compared to the CT solution in the sol form, the viscosity of the solution increases remarkably after injection into simulated body fluid. This is attributed to the reduction in the solubility of CT in an aqueous environment. Owing to their large molecular weight and extensive branching structure, CT molecules entangle with each other, generating a highly porous and compact microstructure via molecular entanglement (Movie S1). Such a network traps a substantial amount of fluids to form a gel at the injection site, and enables CT to be applied as a depot system in subsequent *in vivo* studies.

Apart from changes in viscosity, *in situ* gelation of the CT solution is evidenced in rheological analysis, in which the G' and G'' values are determined by using an oscillatory shear field applied to the sample. G' and G'' values of the CT solutions are found to be much higher after injection into simulated body fluid (Fig. 2C). In all of the gels formed, the G' values are higher than the G'' values. This evidences that the gels exhibit solid-like behavior and are robust. As the gelation process is driven by molecular entanglement, it is expected that by increasing the molecular weight of CT, the extent of molecular entanglement increases, leading to the formation of a gel with higher mechanical strength. This is confirmed by the observation that the G' and G'' values of the gels increases in the order: CT06 < CT15 < CT50, suggesting that an increase in the molecular weight of the polymer enhances the gelation process by more effectively forming a continuous network and hence a firmer gel (Fig. 2D). The microstructure of the gels formed from CT is examined using SEM (Fig. 3A). With an increase in the molecular weight of CT, the level of entanglement per unit volume of the gel increases, leading to the formation of a more compact gel structure. By taking advantage of the microstructural tunability, the swelling behavior (including the swelling ratio, the WAR value, and the water content) and erosion susceptibility of the gel can be changed by manipulating the molecular weight of CT (Fig. 3B-E).

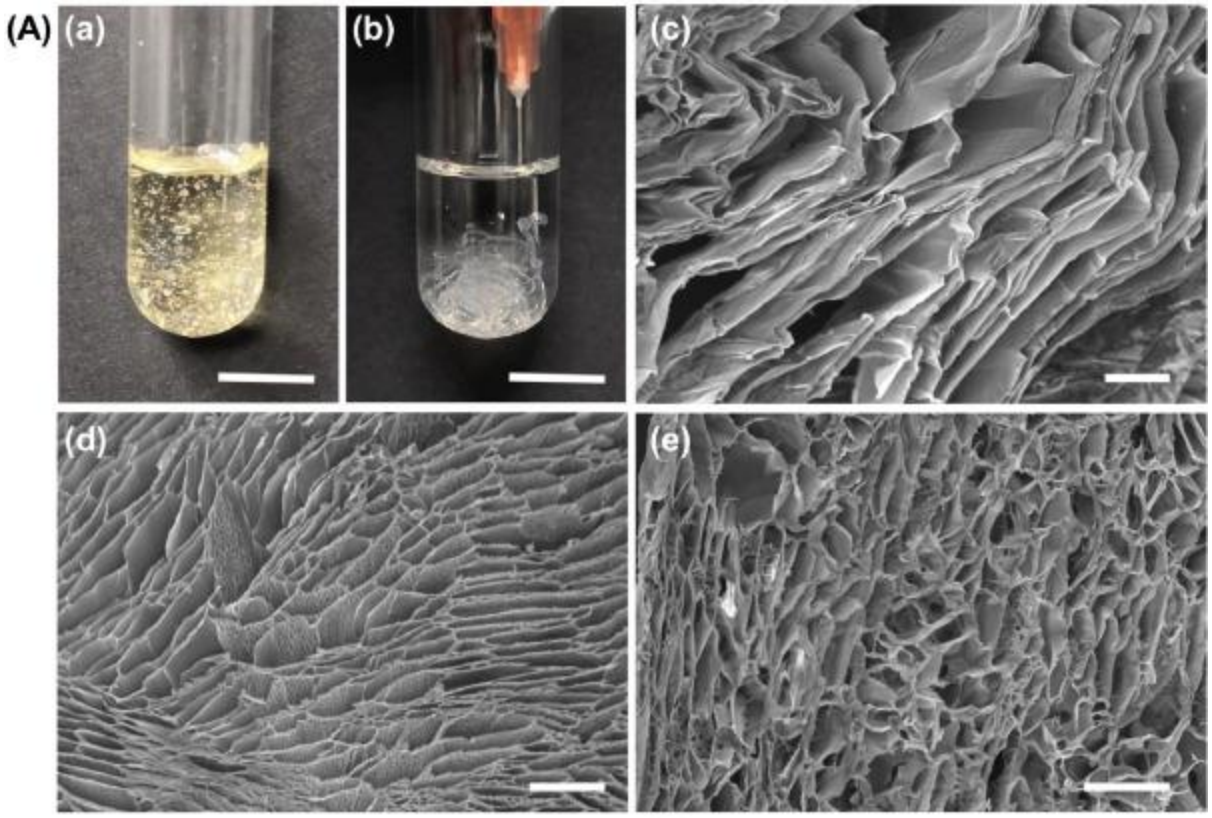
(A)
(a)
(b)
(c)
(d)
(e)

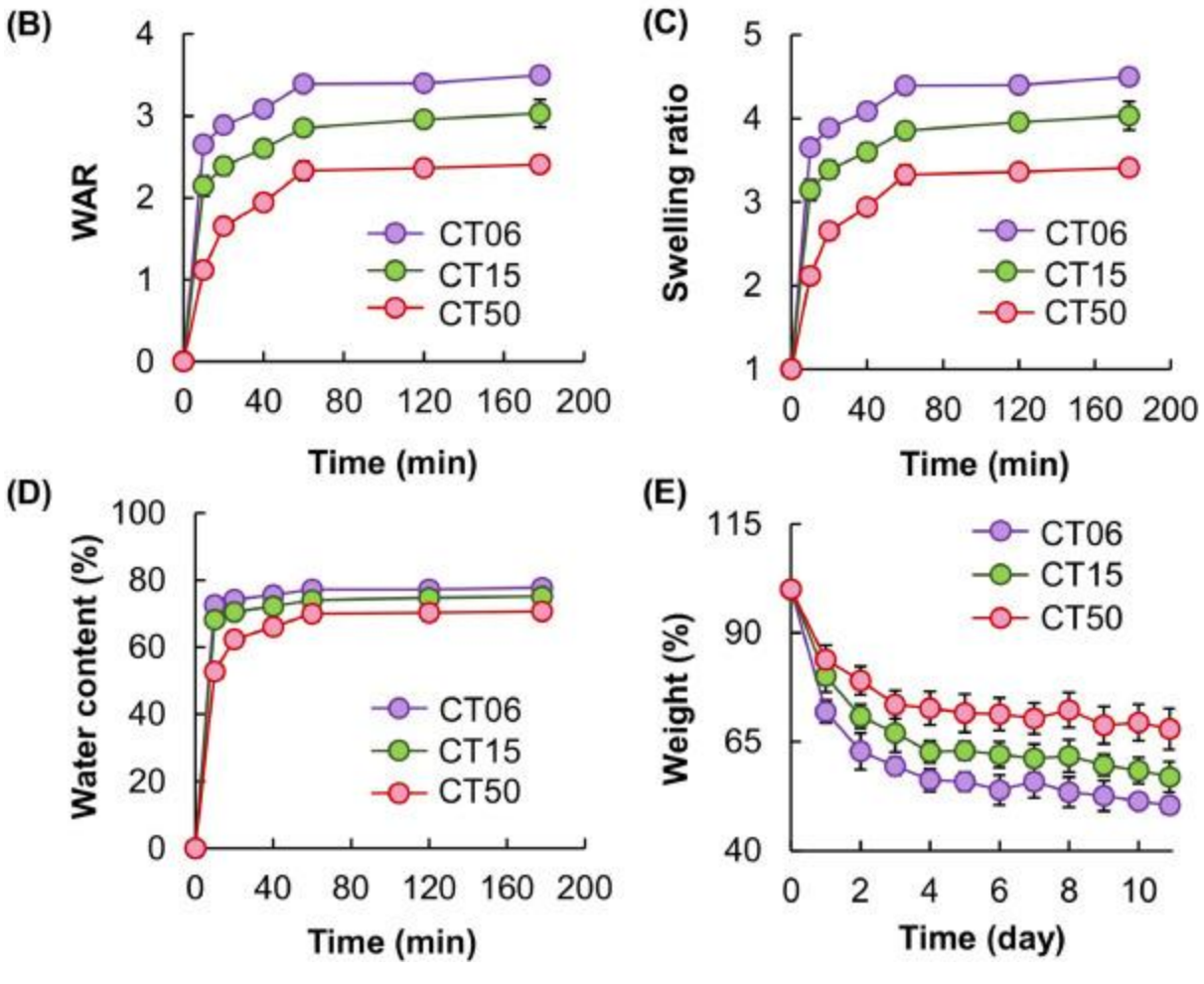
(B)
WAR
Time (min)
CT06
CT15
CT50
(C)
Swelling ratio
Time (min)
CT06
CT15
CT50
(D)
Water content (%)
Time (min)
CT06
CT15
CT50
(E)
Weight (%)
Time (day)
CT06
CT15
CT50

Fig. 3. Swelling and erosion behavior of CT gels. (A) *In situ* gelation of the DMSO solution of CT and the microstructure of the gel formed: (a-b) photos showing (a) the CT solution, and (b) the process of gel formation upon injection into simulated body fluid. Scale bar = 1 cm. (c-e) SEM images of the microstructure of a lyophilized gel formed from (c) CT06, (d) CT15, and (e) CT50. Scale bar = 500 μm. (B) The WAR, (C) the swelling ratio, (D) the water content, and (E) the erosion susceptibility of gels formed from CT with different molecular weights.

3.3. Optical properties of CT

The luminescence of the DMSO solutions of CT under UV irradiation is shown in Fig. 4A. CT displays strong PL upon excitation between 330 nm and 430 nm. The emission peak is rather broad with a full width at half maximum (FWHM) of 100–200 nm (Fig. 4B). CT shows strong excitation wavelength dependence. For CT06, excitation at 330 nm leads to an emission peak at around 440 nm, while excitation at 430 nm shifts the emission peak to 490 nm. This also applies to CT15 and CT50, whose emission peak shifts from 450 to 500 nm, and from 470 to 520 nm, respectively. The average PL lifetime of CT is estimated to be around 4 ns. Depending on the molecular weight of CT, a Stokes shift in the range of 60–140 nm is observed. When the concentration of the CT solution is increased, the luminescence intensity is enhanced (Fig. 4C). This is an important feature of CTE as reported by earlier studies [14], [15], [16], and supports the role played by the entanglement of CT molecules during PL emission. Mechanistically, CTE is an aggregation-induced emission (AIE)-like process caused by interactions among electron-rich heteroatoms (particularly those from functional groups such as C=O, N=O, and C=N) [7]. The occurrence of CTE has previously been reported by a study examining the UV-excited luminescence from oligo(maleic anhydride)s (OMAhs) and poly[(maleic anhydride)-*alt*-(2,4,4-trimethyl-1-pentene)] (PMP) [16]. The luminescence intensity of PMP, in which the maleic anhydride (MAh) repeating units are separated by the bulky *t*-butyl group, has been shown to be lower than that of OMAhs. This observation is caused by the difference in the distance of two adjacent MAh units. The shorter the distance, the more effective the intra-chain non-covalent interactions of the carbonyl groups. Such interactions enable the interpenetration of the lone pair of one carbonyl group into the empty π* orbital of another carbonyl group, resulting in the hybridization of the orbitals and ultimately the release of the excited energy as PL emission [[16], [17]–18]. Apart from OMAhs and PMP, CTE has been observed in non-conjugated natural polymers (such as chitosan [19] and cellulose [20]) via through-space nonbonding interactions among heteroatoms. In fact, the possible occurrence of such interactions between second and third row heteroatoms has already been reported [[21], [22]–23]. These interactions can narrow down the energy gap between the HOMO and LUMO to render the polymer luminescent despite the absence of the conjugated structure [[21], [22], [23]–24].

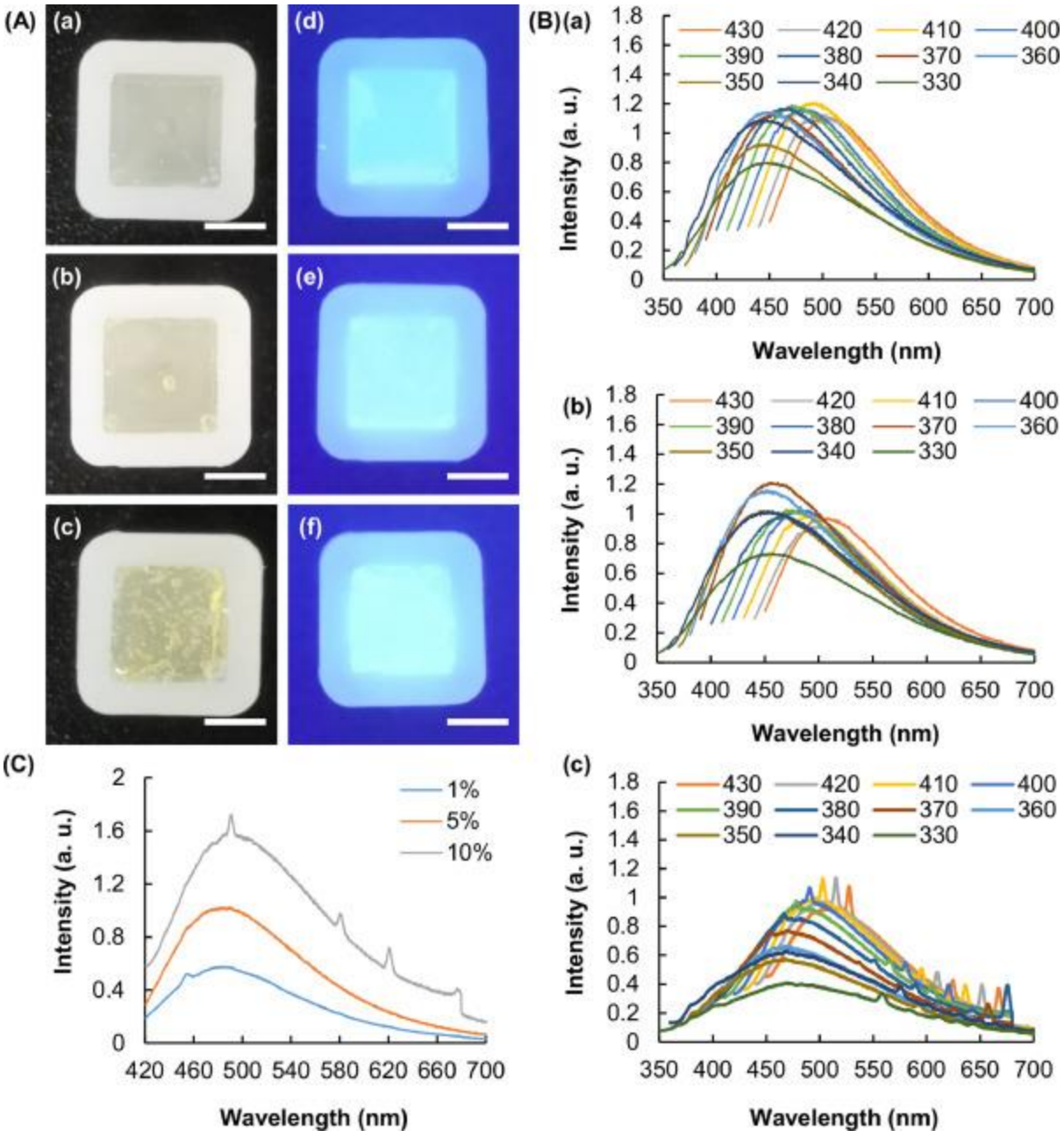

Fig. 4. Optical properties of CT. (A) DMSO solutions of (a, d) CT06, (b, e) CT15 and (c, f) CT50 under (a-c) visible light and (d-f) UV irradiation at 365 nm. Scale bar = 5 mm. (B) PL spectra of DMSO solutions of CT (a, CT06; b, CT15; c, CT50) taken at different excitation wavelengths. (C) PL spectra (λ_{ex} = 400 nm) of DMSO solutions containing different (w/v) concentrations of CT15.

Due to the occurrence of CTE, an increase in the luminescence intensity of the CT solutions is observed when an increasing amount of simulated body fluid is added to induce gel formation (Fig. 5A-B). As the process of gelation proceeds, the intensity of the luminescence is enhanced, too (Fig. 5C-D). The potential use of this unique optical property in *in vivo* tracking of CT is evidenced by using nude mice as a model. Upon IP

injection of the CT solution, *in situ* gelation is initiated, leading not only to the formation of a gel as a depot of bioactive agents within 24 min after injection (Fig. 5E-F) but also to the enhancement of the luminescence intensity. The latter enables the gel to be successfully located via *in vivo* imaging techniques, with the gelation process being monitored in real time. Along with the excitation wavelength-dependent emission tunability of CT, the gel can function as a tunable light-emitting device in a body, with its size and location being able to be tracked optically during subsequent self-illuminating antitumor therapy.

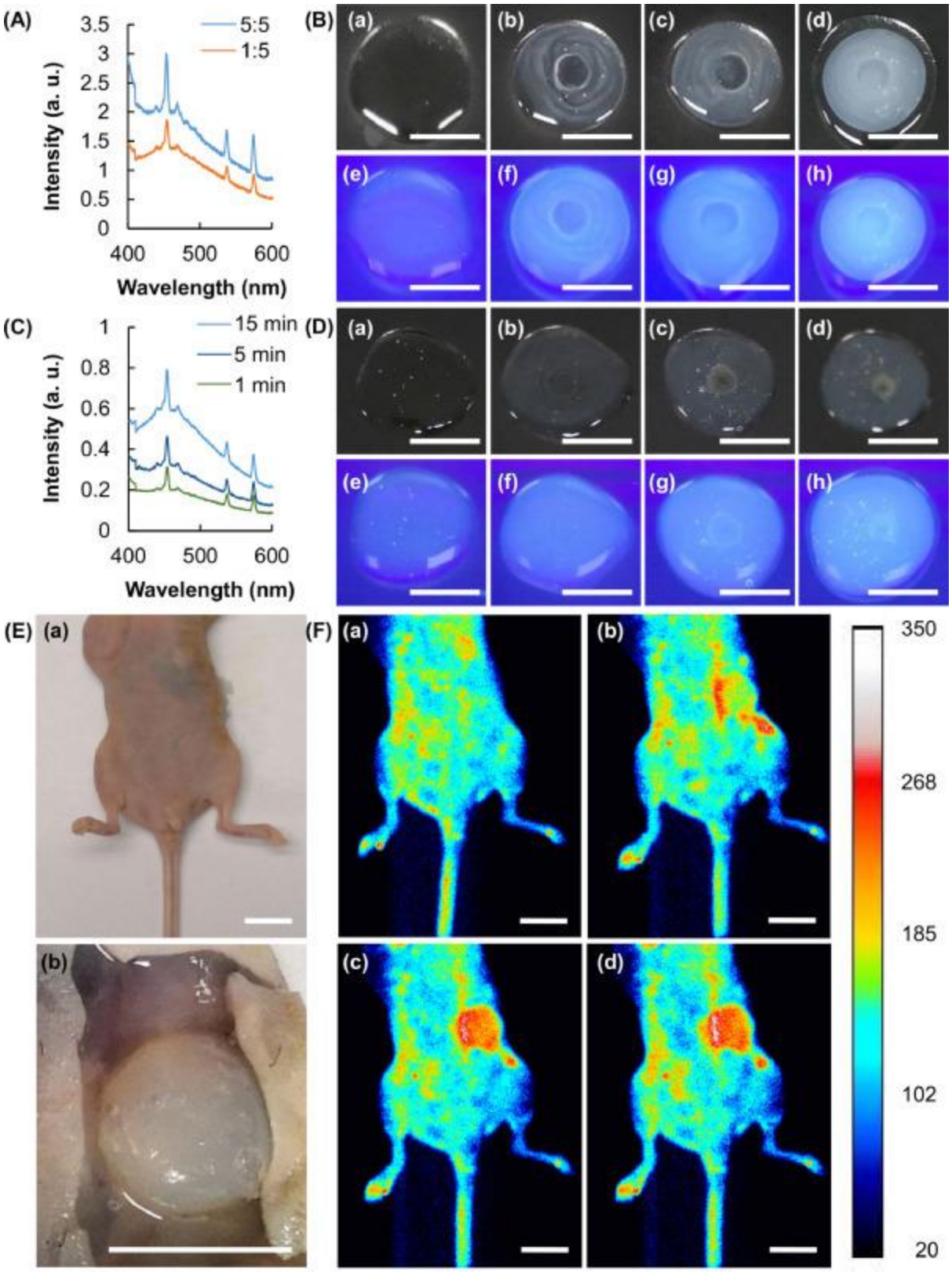
(A)
Intensity (a. u.)
Wavelength (nm)
5:5
1:5
(B)
(a)
(b)
(c)
(d)
(e)
(f)
(g)
(h)
(C)
Intensity (a. u.)
Wavelength (nm)
15 min
5 min
1 min
(D)
(E)
(F)
350
268
185
102
20

Fig. 5. *In situ* gelation of CT and optical tracking. (A) PL spectra (λ_{ex} = 370 nm) of DMSO solutions of CT15 upon the addition of simulated body fluid at different simulated body fluid/DMSO volume-to-volume ratios. (B) (a-d) Visible light and (e-h) UV images of a droplet of the CT15 solution after the addition of simulated body fluid at different simulated body fluid/DMSO volume-to-volume ratios (a, e, 0:5; b, f, 1:5; c, g, 3:5; d, h, 5:5). Scale bar = 1 cm. (C) PL spectra (λ_{ex} = 370 nm) of a DMSO solution of CT15 taken at different time intervals after the addition of simulated body fluid. The volume-to-volume ratio of the CT15 solution and simulated body fluid is 1:1. (D) (a-d) Visible light and (e-h) UV images of a droplet of the CT15 solution taken at different time intervals (a, e, 0 min; b, f, 1 min; c, g, 5 min; d, h, 15 min) after the addition of simulated body fluid. The volume-to-volume ratio of the CT15 solution and simulated body fluid is 1:1. Scale bar = 1 cm. (E) (a) The visible light image of the abdomen of a nude mice after IP injection of the CT solution, and (b) the visible light image of the *in situ*-formed gel exposed upon skin removal. (F) UV images of the abdomen of a nude mice after IP injection of the CT solution. The images are taken (a) 0 min, (b) 6 min, (c) 12 min, and (d) 24 min after the injection procedure. Scale bar = 1 cm.

3.4. Performance of CT as a depot of bioactive agents

The process of molecular entanglement in an aqueous environment enables CT to form a depot of bioactive agents *in situ* (Fig. 6A). MB, LYS, CAP, and PTX are adopted as model agents in this study. Depending on the solubility and molecular weight of the agent to be loaded, the encapsulation efficiency of the gel formed from CT reaches 30–90% (Fig. 6B). The release sustainability of a gel has been shown by previous studies to be affected not only by the aqueous solubility of the loaded agent but also by the swelling and erosion behavior of the gel [25,26]. The latter is attributed to the fact that the release of the loaded agent (particularly hydrophilic ones) from a matrix-type device is generally driven by Fickian diffusion, which is governed largely by the degree of swelling of the device [27]. In the case of CT gels, the swelling capacity and erosion susceptibility can be tuned by changing the microstructure, which in turn can be controlled by changing the size of the polymer molecule (Fig. 3). The release sustainability of CT gels can, therefore, be manipulated by changing the molecular weight of CT (Fig. 6C). Furthermore, because the rate of diffusion of the loaded agent from the gels to the releasing medium is affected by the size of the agent molecule [[28], [29]–30] and by the affinity of the agent to the gel matrix [25,31], the release rate varies with the model agent adopted.

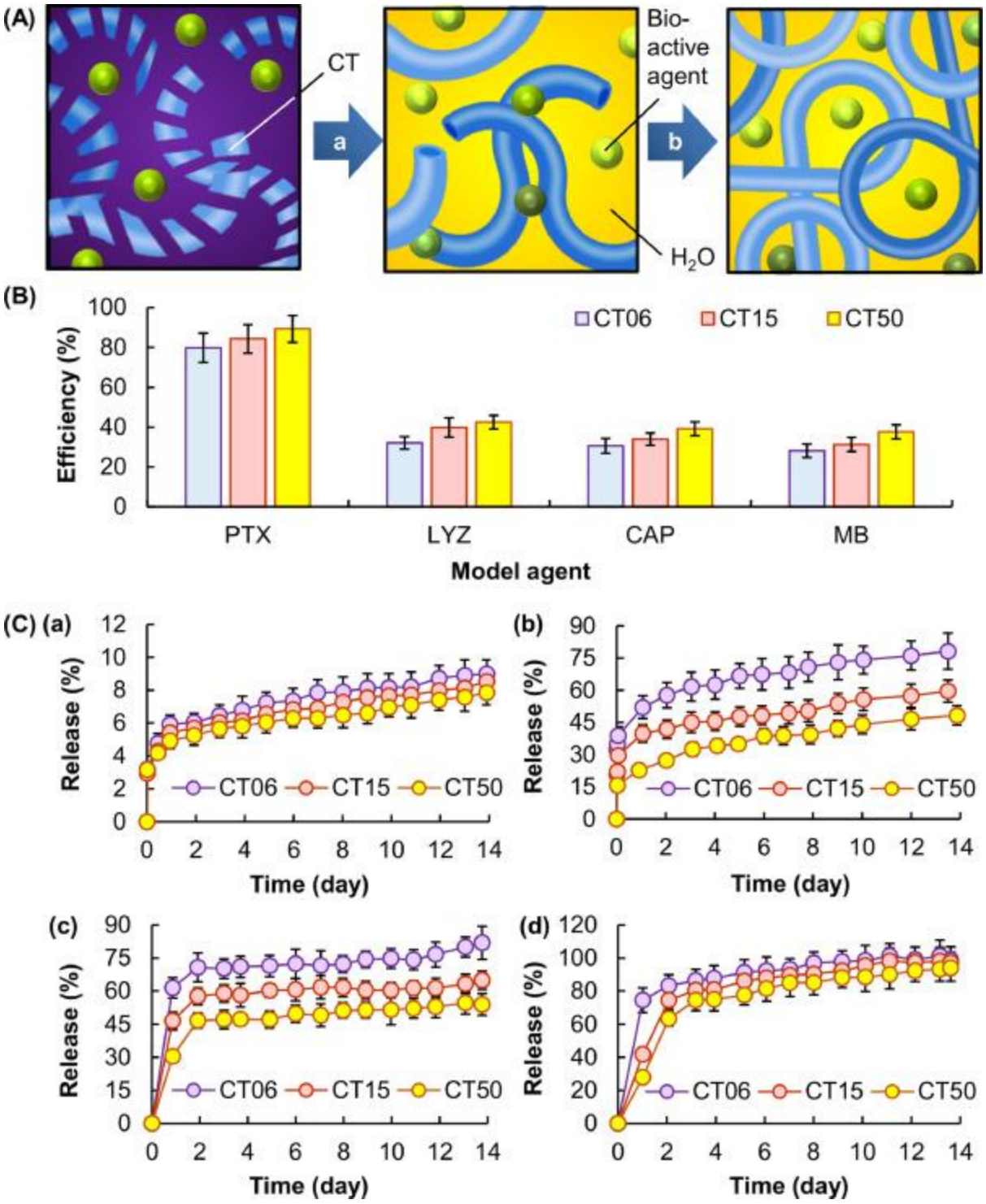

Fig. 6. Performance of CT as a depot system for bioactive agent delivery. (A) A schematic diagram showing the formation of a depot of bioactive agents via (a) precipitation and (b) molecular entanglement of CT molecules upon injection of a DMSO solution of CT into an aqueous environment. (B) The encapsulation efficiency of gels formed from CT with different molecular weights. (C) Release profiles of (a) PTX, (b) LYS, (c) CAP, and (d) MB from gels formed from CT with different molecular weights.

In order for a gel system to be applicable as a bioactive agent carrier, the capacity of maintaining the activity of the agent after the loading process is required [28,30,32]. Unlike gels formed by chemical crosslinking in which exposure of the loaded agent to the crosslinking reaction may compromise the agent stability [[33], [34]–35], the smart response of CT to the surrounding medium for *in situ* gel formation allows the gelation process to occur under mild conditions without necessitating the artificial provision of irradiation or any other physical/chemical initiators. To demonstrate the ability of the CT gel to maintain the activity of the loaded agent, LYS is used. It is a protein that can hydrolyze β(1→4) linkages between N-acetyl-D-glucosamine residues in chitodextrin, and between N-acetyl-D-glucosamine and N-acetylmuramic acid residues in peptidoglycan [36]. Because of its labile protein nature, it is highly susceptible to inactivation and conformational destabilization upon different stimuli (ranging from aggregation and heat to chemical denaturation). This makes LYS an ideal model to evaluate the possible effect imposed by gel encapsulation on the activity of the loaded agent. As revealed by the high rate of lysis of the gram-positive bacteria *Micrococcus lysodeikticus* (which is vulnerable to hydrolysis mediated by lysozyme because of the presence of a high level of peptidoglycan in its cell wall) (Fig. 7A-B), the activity level of LYS is high (over 80%) after the loading process. This suggests that the effect of encapsulation by the CT gel on the activity of the loaded agent is insignificant.

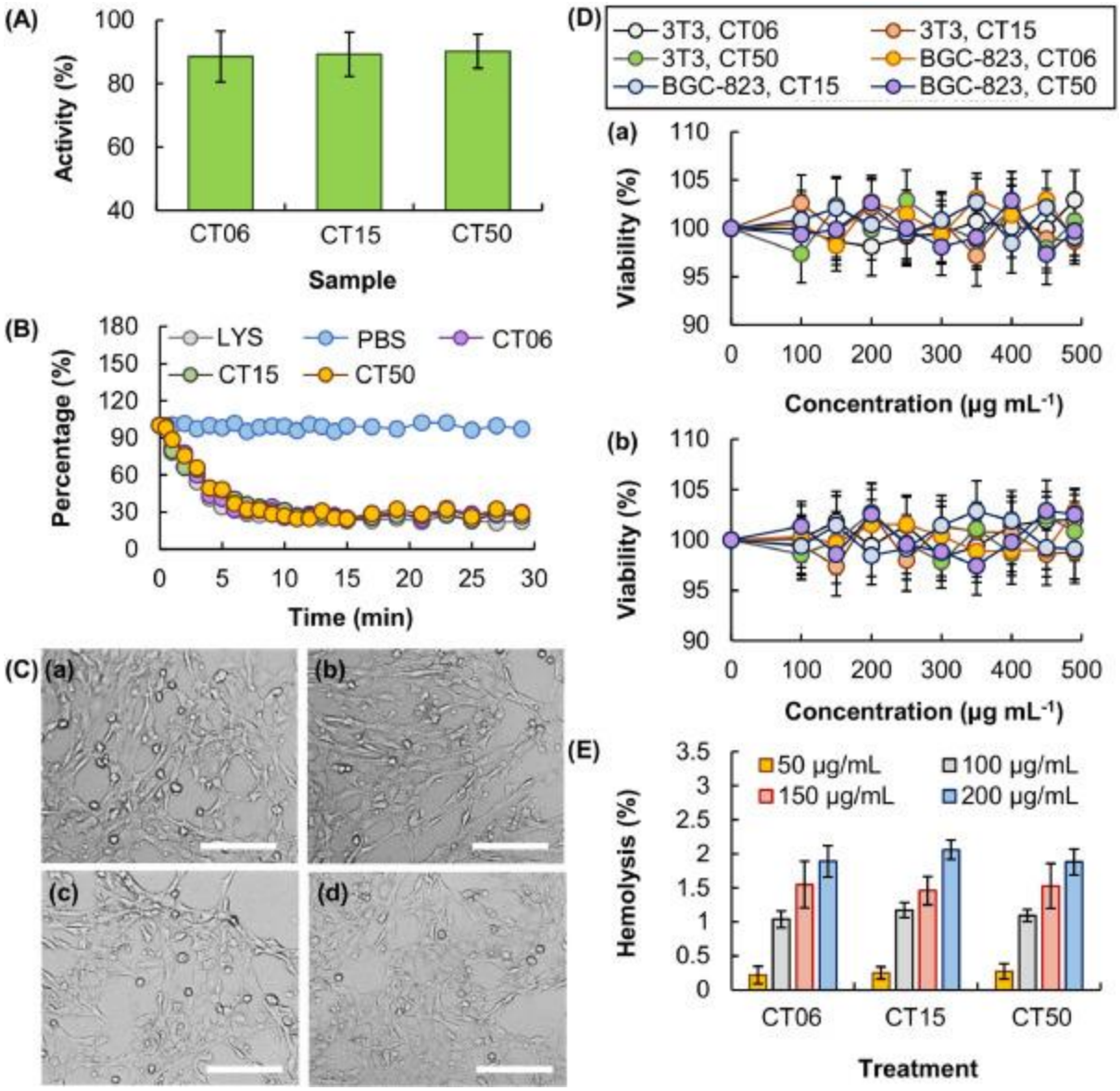

Fig. 7. Biocompatibility of CT as a carrier of bioactive agents. (A) The antibacterial activity of LYS extracted from gels formed from CT with different molecular weights. The activity of pure lysozyme is taken as 100%. (B) Time-dependent changes in the content of *Micrococcus lysodeikticus* after the addition of LYS extracted from different CT gels. The LYS solution and PBS are used as the controls. (C) Optical images of 3T3 fibroblasts after 5 h treatment with (a) PBS, (b) CT06, (c) CT15 and (d) CT50. Scale bar = 200 μm. (D) Viability of 3T3 fibroblasts and BGC-823 cells after 5 h treatment with different concentrations of CT, (a) without or (b) with 24 h post-treatment incubation. (E) Percentages of erythrocytes lysed upon treatment with different concentrations of CT.

Finally, the safety profile of CT is evaluated in 3T3 fibroblasts. No apparent change in cell morphology is observed after 5 h treatment with CT06, CT15 and CT50 (Fig. 7C). The low cytotoxicity of CT is further confirmed by using the MTS assay, which reveals that the loss of cell viability after 5 h treatment with the CT polymers is negligible in all concentrations

tested (Fig. 7Da). To determine potential chronic cytotoxicity, the viability of the treated cells is examined after 24 h post-treatment incubation. No significant loss of cell viability is observed (Fig. 7Db). Apart from 3T3 cells, the cytotoxicity assay is performed in BGC-823 cells, which are adopted to establish the xenograft model for studying the use of CT in self-illuminating antitumor therapy, so as to ensure that any therapeutic effect observed in the subsequent part of this study is due to the efficiency of CT as a carrier rather than due to the toxic effect of CT *per se*. Both acute and chronic cytotoxicity of CT are found to be negligible in all concentrations tested (Fig. 7D). Apart from its low cytotoxicity, CT exhibits high biocompatibility as demonstrated by its low hemolytic activity (Fig. 7E). All these corroborate the high safety profile of CT for biomedical use.

3.5. Applications in self-illuminating antitumor therapy

To illustrate the application potential of CT in self-illuminating antitumor therapy, a mouse xenograft model established by using BGC-823 cells is adopted. PTX is employed to mediate the therapy due to its track record of effectiveness against a variety of human cancers [37]. Upon administration of the PTX-containing CT solution into the tumor site, rapid phase inversion from a solution to a hardened depot matrix is induced. This forms a depot of bioactive agents *in situ* to localize the delivery site and to enable sustained PTX release. The use of CT as a carrier remarkably enhances the antitumor effect, with the size of the tumor in the CT/PTX group being the smallest among all treatment groups (Fig. 8A). Histological analysis shows that the number of Ki67 positive cells is significantly reduced by treatment with the PTX-containing CT solution (Fig. 8B), which also causes the absence of the morphological features of normal gastric cancer cells in the tumor section obtained from the treated mice (Fig. 8C).

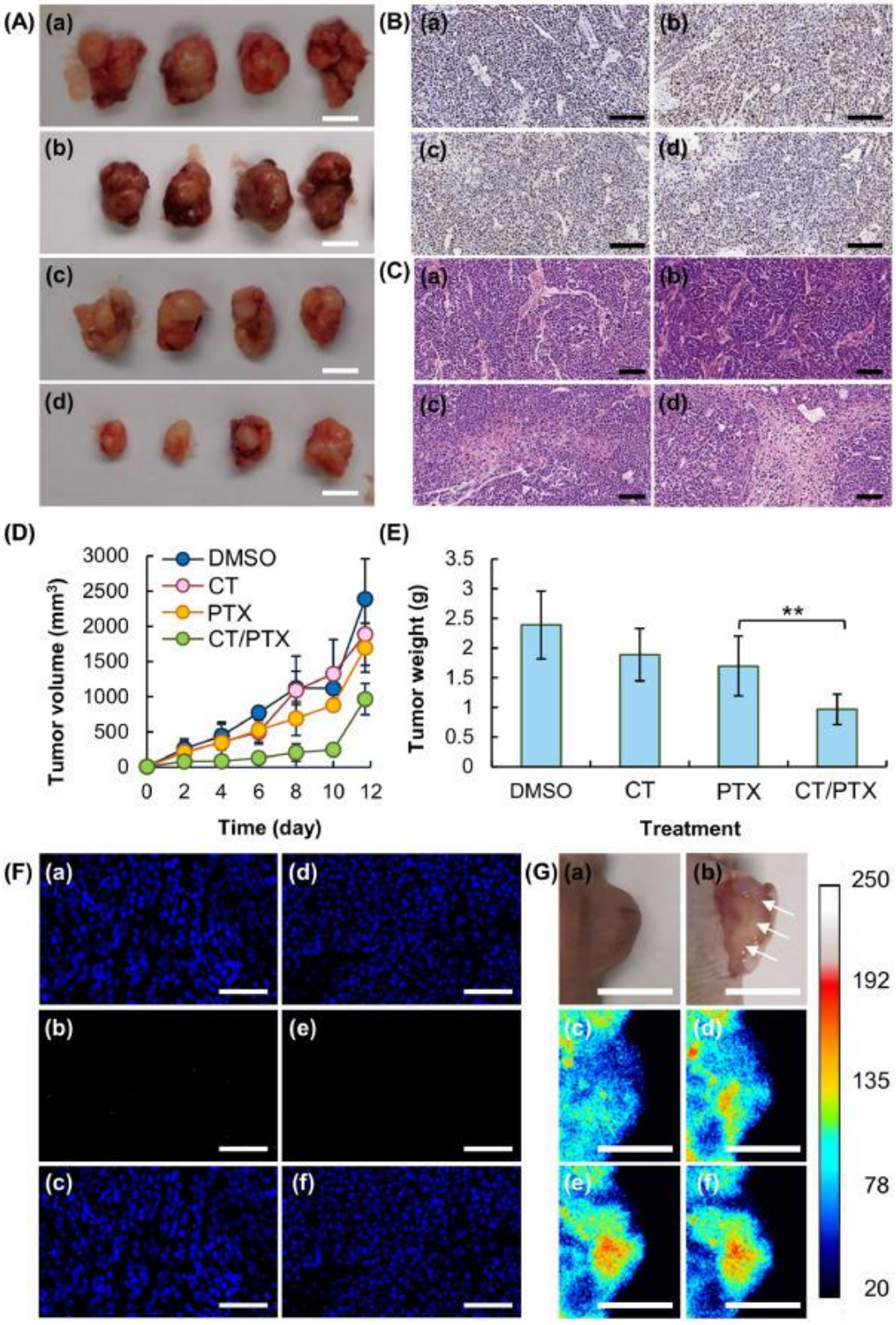

Fig. 8. Applications of CT in real-time self-illuminating antitumor therapy (A) Images of tumors dissected from mice in different groups: (a) control, (b) CT, (c) PTX, and (d)

CT/PTX. Scale bar = 1 cm. (B) Representative images of the Ki67-stained tumor sections obtained from different groups: (a) DMSO, (b) CT, (c) PTX, and (d) CT/PTX. Scale bar = 100 μm (C) Representative images of the H&E-stained tumor sections obtained from different groups: (a) DMSO, (b) CT, (c) PTX, and (d) CT/PTX. Scale bar = 100 μm (D) Changes in the tumor volume of mice in different treatment groups. (E) Average weights of the tumors dissected on day 12 from mice in different treatment groups. ** denotes $p < 0.01$. (F) Representatives images of tumor sections stained with (a, d) 4,6-diamidino-2-phenylindole (DAPI) and (b, e) a green TUNEL stain, as well as their (c, f) merged images, from mice treated with (a-c) DMSO and the (d-f) CT solution. Scale bar = 100 μm. (G) Visible light images of (a) the tumor after intratumoral injection of a PTX-containing CT solution and (b) the gel formed *in situ* inside the tumor (with the location of the gel indicated by white arrows), as well as the (c-f) UV images of the tumor in a nude mouse. The UV images are taken (a) 0 min, (b) 6 min, (c) 12 min, and (d) 24 min after intratumoral injection of a PTX-containing CT solution. Scale bar = 5 mm.

To quantitatively evaluate the efficiency of the antitumor therapy mediated by CT as an *in situ*-forming PTX depot, the TGI values in different treatment groups are determined. Compared to mice in the control group, those in the CT, PTX, and CT/PTX groups have TGI values of 21.1%, 29.0%, and 59.0%, respectively. Mice treated with the PTX-containing solution experience a substantial reduction in the tumor volume and the tumor weight (Fig. 8D-E), with the latter being only 60% of that of mice treated directly with the PTX solution. This demonstrates the efficiency of CT in enhancing the performance of the therapy. Results of the TUNEL assay reveal that the CT solution alone induces no observable increase in apoptosis of tumor cells as compared to the control (Fig. 8F). This reveals the high biocompatibility of CT, and is consistent with the *in vitro* findings reported in the preceding section, in which CT shows negligible cytotoxic effects, both acute and chronic, in BGC-823 cells (Fig. 7D). Apart from the capacity of enhancing the therapeutic effect in treatment, by taking advantage of the CTE property and the excitation wavelength-dependent emission tunability of CT, the size, location and *in situ* formation of the PTX depot are successfully monitored in real time (Fig. 8G). This enables CT to function as a tunable light-emitting depot in a body, with its size and location being able to be tracked optically during the therapy.

4. Conclusion

Development of sustained-release carriers possessing intrinsic luminescence can enhance the combination of imaging with bioactive agent delivery in practice. This study reports the synthesis and properties of a biocompatible, gel-forming and highly tunable polymer, namely CT. The encapsulation efficiency and release sustainability of the gel formed can be tuned by changing the molecular weight of the polymer. Due to its unique CTE property and excitation wavelength-dependent emission tunability, CT enables *in vivo* optical tracking, with its use not being hindered by the limitations (*e.g.*, aggregation-caused quenching, and the need of laborious synthetic procedures) encountered by conventional polymeric luminogens. To the best of our knowledge, this study is the first proof-of-concept study demonstrating the feasibility of integrating CTE of the non-conjugated polymer into carrier design for execution of self-illuminating antitumor therapy. The therapy is currently tested only in the *in vivo* context. Few technical challenges may have

to be overcome before the therapy can be translated into clinical reality. One of these challenges is the need to search for a more biocompatible organic solvent alternative to anhydrous DMSO for dissolution of CT. This can enhance the safe use of the polymer in practice. In addition, only intratumoral injection is tested in this study for execution of the CT-mediated antitumor therapy. The performance of the therapy administered via different routes is required to be tested so as to extend the applicability of the material in antitumor therapy. Finally, excitation of CT in this study is mediated by UV or visible blue light, which shows limited tissue penetration and may cause detrimental photochemical reactions [38]. Further understanding of the mechanism underlying CTE may help provide insights into strategies to tune the excitation and emission profiles of CT so that interference from tissues can be reduced during optical tracking. Notwithstanding these challenges to be solved, based on its high biocompatibility and effective performance, CT shows high practical potential to serve as a prototype for further development of carriers that enable tracking of the delivery process in real time.

Movie S1. *In situ* gelation of the CT solution via molecular entanglement upon injection into simulated body fluid.

Data availability

All data needed to evaluate the conclusions in the paper are present in the paper and/or the Supplementary Materials. Additional data related to this paper may be requested from the authors.

Declaration of Competing Interest

The authors declare that they have no known competing financial interests or personal relationships that could have appeared to influence the work reported in this paper.

References

[1] A. Roy, S. Jhunjhunwala, E. Bayer, M. Fedorchak, S.R. Little, P.N. Kumta, Porous calcium phosphate-poly (lactic-co-glycolic) acid composite bone cement: a viable tunable drug delivery system, Mater. Sci. Eng. C Mater. Biol. Appl. 59 (2016) 92–101.
[2] P. Tipduangta, P. Belton, L. Fabian, L.Y. Wang, H. Tang, M. Eddleston, S. Qi, Electrospun polymer blend nanofibers for tunable drug delivery: the role of transformative phase separation on controlling the release rate, Mol. Pharm. 13 (1) (2016) 25–39.
[3] E. Mauri, F. Rossi, A. Sacchetti, Tunable drug delivery using chemoselective functionalization of hydrogels, Mater. Sci. Eng. C Mater. Biol. Appl. 61 (2016) 851–857.
[4] A. Al Samad, A. Bethry, E. Koziolova, M. Netopilik, T. Etrych, Y. Bakkour, J. Coudane, F. El Omar, B. Nottelet, PCL-PEG graft copolymers with tunable amphiphilicity as efficient drug delivery systems, J. Mater. Chem. B 4 (37) (2016) 6228–6239.
[5] Y. Li, N. Li, W. Pan, Z. Yu, L. Yang, B. Tang, Hollow mesoporous silica nanoparticles with tunable structures for controlled drug delivery, ACS Appl. Mater. Interfaces 9 (3) (2017) 2123–2129.
[6] L.M. Suta, A. Tudor, C.R. Sandulovici, L. Stelea, D. Hadaruga, C. Mircioiu, G. S. Balint, Multivariate statistical analysis regarding the formulation of oxicam-based pharmaceutical hydrogels, Rev. Chim. 68 (4) (2017) 726–731.

[7] R. Lopez-Cebral, P. Paolicelli, V. Romero-Caamano, B. Seijo, M.A. Casadei, A. Sanchez, Spermidine-cross-linked hydrogels as novel potential platforms for pharmaceutical applications, J. Pharm. Sci. 102 (8) (2013) 2632–2643.
[8] W. Farhat, R. Venditti, N. Mignard, M. Taha, F. Becquart, A. Ayoub, Polysaccharides and lignin based hydrogels with potential pharmaceutical use as a drug delivery system produced by a reactive extrusion process, Int. J. Biol. Macromol. 104 (2017) 564–575.
[9] C.S.A. de Lima, T.S. Balogh, J.P.R.O. Varca, G.H.C. Varca, A.B. Lugao, L. A. Camacho-Cruz, E. Bucio, S.S. Kadlubowski, An updated review of macro, micro, and nanostructured hydrogels for biomedical and pharmaceutical applications, Pharmaceutics 12 (10) (2020) 970.
[10] L.S. Liu, J. Kost, F. Yan, R.C. Spiro, Hydrogels from biopolymer hybrid for biomedical, food, and functional food applications, Polymers 4 (2) (2012) 997–1011.
[11] M.S. Lindblad, A.C. Albertsson, New materials based on hemicelluloses: hydrogels and food delivery materials, Abstr. Pap. Am. Chem. Soc. 227 (2004) U282–U283.
[12] S. Farris, K.M. Schaich, L.S. Liu, L. Piergiovanni, K.L. Yam, Development of polyion-complex hydrogels as an alternative approach for the production of bio- based polymers for food packaging applications: a review, Trends Food Sci. Technol. 20 (8) (2009) 316–332.
[13] B. Stella, I. Andreana, D. Zonari, S. Arpicco, Pentamidine-loaded lipid and polymer nanocarriers as tunable anticancer drug delivery systems, J. Pharm. Sci. 109 (3) (2020) 1297–1302.
[14] A. Passi, D. Vigetti, Hyaluronan as tunable drug delivery system, Adv. Drug Deliv. Rev. 146 (2019) 83–96.
[15] W.F. Lai, C. Hu, G. Deng, K.H. Lui, X. Wang, T.H. Tsoi, S. Wang, W.T. Wong, A biocompatible and easy-to-make polyelectrolyte dressing with tunable drug delivery properties for wound care, Int. J. Pharm. 566 (2019) 101–110.
[16] R.C.F. Goncalves Lopes, O.F. Silvestre, A.R. Faria, C.d.V. Ml, E.F. Marques, J. B. Nieder, Surface charge tunable catanionic vesicles based on serine-derived surfactants as efficient nanocarriers for the delivery of the anticancer drug doxorubicin, Nanoscale 11 (13) (2019) 5932–5941.
[17] S.R. Abulateefeh, M.Y. Alkawareek, A.M. Alkilany, Tunable sustained release drug delivery system based on mononuclear aqueous core-polymer shell microcapsules, Int. J. Pharm. 558 (2019) 291–298.
[18] W.F. Lai, A.S. Susha, A.L. Rogach, Multicompartment microgel beads for co-delivery of multiple drugs at individual release rates, ACS Appl. Mater. Interfaces 8 (1) (2016) 871–880.
[19] W.F. Lai, E. Huang, K.H. Lui, Alginate-based complex fibers with the Janus morphology for controlled release of co-delivered drugs, Asian J. Pharm. Sci. (2020), https://doi.org/10.1016/j.ajps.2020.05.003.
[20] W.F. Lai, A.L. Rogach, W.T. Wong, One-pot synthesis of an emulsion-templated hydrogel-microsphere composite with tunable properties, Compos. Part A-Appl. S. 113 (2018) 318–329.
[21] W.F. Lai, E. Huang, W.T. Wong, A gel-forming clusteroluminogenic polymer with tunable emission behavior as a sustained-release carrier enabling real-time tracking during bioactive agent delivery, Appl. Mater. Today 21 (2020) 100876.

[22] W.F. Lai, H.C. Shum, A stimuli-responsive nanoparticulate system using poly(ethylenimine)-graft-polysorbate for controlled protein release, Nanoscale 8(1) 517-528.
[23] W.F. Lai, H.C. Shum, Hypromellose-graft-chitosan and its polyelectrolyte complex as novel systems for sustained drug delivery, ACS Appl. Mater. Interfaces 7(19) 10501-10510.
[24] L. Viglianti, N.L.C. Leung, N. Xie, X.G. Gu, H.H.Y. Sung, Q. Miao, I.D. Williams, E. Licandro, B.Z. Tang, Aggregation-induced emission: mechanistic study of the clusteroluminescence of tetrathienylethene, Chem. Sci. 8 (4) (2017) 2629–2639.
[25] W.F. Lai, Non-conjugated polymers with intrinsic luminescence for drug delivery, J. Drug Deliv. Sci. Technol. 59 (2020) 101916.
[26] R. Hoffmann, Interaction of orbitals through space and through bonds, Acc. Chem. Res. 4 (1) (1971) 1–9.
[27] X.G. Guo, J. Quinn, Z.H. Chen, H. Usta, Y. Zheng, Y. Xia, J.W. Hennek, R.P. Ortiz, T.J. Marks, A. Facchetti, Dialkoxybithiazole: a new building block for head-to-head polymer semiconductors, J. Am. Chem. Soc. 135 (5) (2013) 1986–1996.
[28] N. Hergue, C. Mallet, G. Savitha, M. Allain, P. Frere, J. Roncali, Facile synthesis of 3-alkoxy-4-cyanothiophenes as new building blocks for donor-acceptor conjugated systems, Org. Lett. 13 (7) (2011) 1762–1765.
[29] A.S. Ozen, C. Atilgan, G. Sonmez, Noncovalent intramolecular interactions in the monomers and oligomers of the acceptor and donor type of low band gap conducting polymers, J. Phys. Chem. C 111 (44) (2007) 16362–16371.
[30] I.S.M. Zaidul, T.K. Fahim, F. Sahena, A.K. Azad, M.A. Rashid, M.S. Hossain, Dataset on applying HPMC polymer to improve encapsulation efficiency and stability of the fish oil: in vitro evaluation, Data Brief 32 (2020) 106111.
[31] W.F. Lai, A.S. Susha, A.L. Rogach, G.A. Wang, M.J. Huang, W.J. Hu, W.T. Wong, Electrospray-mediated preparation of compositionally homogeneous core-shell hydrogel microspheres for sustained drug release, RSC Adv. 7 (70) (2017) 44482–44491.
[32] W.F. Lai, A.L. Rogach, Hydrogel-based materials for delivery of herbal medicines, ACS Appl. Mater. Interfaces 9 (13) (2017) 11309–11320.
[33] W.F. Lai, Z.D. He, Design and fabrication of hydrogel-based nanoparticulate systems for in vivo drug delivery, J. Contr. Release 243 (2016) 269–282.
[34] Y.Q. Zhang, J.F. Zhang, Y.J. Xiao, V.W.C. Chang, T.T. Lim, Direct and indirect photodegradation pathways of cytostatic drugs under UV germicidal irradiation: process kinetics and influences of water matrix species and oxidant dosing, J. Hazard Mater. 324 (2017) 481–488.
[35] M. Litvic, K. Smic, V. Vinkovic, M. Filipan-Litvic, A study of photodegradation of drug rosuvastatin calcium in solid state and solution under UV and visible light irradiation: the influence of certain dyes as efficient stabilizers, J. Photochem. Photobiol., A 252 (2013) 84–92.
[36] S. Sijak, N. Liu, M. Zheng, G. Xu, L. Tang, J.Z. Yao, M.H. Wu, Degradation of anticonvulsant drug primidone in aqueous solution by UV photooxidation processes, Environ. Eng. Sci. 32 (5) (2015) 436–444.
[37] J. Siepmann, F. Siepmann, Mathematical modeling of drug delivery, Int. J. Pharm. 364 (2) (2008) 328–343.